Towards Left Ventricular Scar Localisation Using Local Motion Descriptors

Devis Peressutti[1(✉)], Wenjia Bai[2], Wenzhe Shi[2], Catalina Tobon-Gomez[1], Thomas Jackson[1], Manav Sohal[1], Aldo Rinaldi[1], Daniel Rueckert[2], and Andrew King[1]

[1] Division of Imaging Sciences and Biomedical Engineering, King's College London, London, UK
devis.1.peressutti@kcl.ac.uk
[2] Biomedical Image Analysis Group, Imperial College London, London, UK

Abstract. We propose a novel technique for the localisation of Left Ventricular (LV) scar based on local motion descriptors. Cardiac MR imaging is employed to construct a spatio-temporal motion atlas where the LV motion of different subjects can be directly compared. Local motion descriptors are derived from the motion atlas and dictionary learning is used for scar classification. Preliminary results on a cohort of 20 patients show a sensitivity and specificity of 80 % and 87 % in a binary classification setting.

1 Introduction

Accurate assessment of Left Ventricular (LV) scar location is paramount in many clinical applications, ranging from the evaluation of viable LV myocardium following myocardial infarction, to the planning of optimal lead placement in Cardiac Resynchronisation Therapy (CRT) or cardiac stem cells transplant [1,10].

Cardiac Magnetic Resonance (CMR) has become the imaging modality of choice for the characterisation of cardiac function and scar distribution due to its high spatial resolution, soft-tissue contrast and non-invasiveness. In particular, delayed-enhancement MR (DE-MR) imaging allows evaluation of the extent of scarred myocardium after injection of a contrast agent [10]. In DE-MR, scarred areas appear hyper-enhanced compared to healthy myocardium and scar transmurality is typically quantified by manually adjusting an intensity threshold. Standard clinical DE-MR protocols typically acquire 2D short-axis (SA) and long-axis (LA) images of the LV with slice thickness $\approx 10\,mm$, and therefore lack accurate through-plane scar information. Furthermore, DE-MR requires the use of a contrast agent, which is typically a gadolinium-based nephrotoxic drug.

Injured myocardium alters LV electrical activation and mechanical contraction, which causes differences in LV motion between ischaemic and non-ischaemic myocardium [7]. We present a framework for the prediction of LV scar location purely based on LV motion, without the need for a DE-MR scan or user interaction. We present preliminary results on a cohort of patients selected for CRT,

O. Camara et al. (Eds.): STACOM 2015, LNCS 9534, pp. 30–39, 2016.
DOI: 10.1007/978-3-319-28712-6_4

but the proposed framework has potential use in the assessment of LV scar distribution for other applications. To the authors' knowledge, very little work has been done on the use of 3D LV motion for automatic localisation of scar. Related work includes [8], in which the cardiac shape at different cardiac phases was used to characterise scarred myocardium, although it should be noted that their best results were achieved using the shape at only a single phase (end systole).

In the proposed method, LV motion is estimated using (T-MR) imaging, which provides 3D high-spatial resolution motion information. A spatio-temporal motion atlas is generated to remove biases towards LV geometry and cardiac cycle duration, allowing direct comparison of the LV motions of different patients. The novelty of our method lies in the use of local motion descriptors and dictionary learning to localise scar. Provided with the 3D LV motion descriptors of an unseen patient, the proposed framework is able to predict location of scarred myocardium.

2 Materials

A cohort of 20 patients[1] fulfilling conventional criteria for CRT (New York Heart Association functional classes II to IV, QRS duration $> 120\,ms$, and LV ejection fraction $\leq 35\,\%$) was considered. All patients underwent CMR imaging using a 1.5 T scanner (Achieva, Philips Healthcare, Best, Netherlands) with a 32-element cardiac coil. Details of the acquired CMR sequences are as follows:

cine MR: a multi-slice SA and three single-slice LA (2-chamber, 3-chamber and 4-chamber view) 2D cine Steady State Free Precession (SSFP) sequences were acquired (TR/TE = $3.0/1.5\,ms$, flip angle = $60°$). The SA and LA images have a typical slice thickness of $8\,mm$ and $10\,mm$, respectively and an in-plane resolution $\approx 1.4 \times 1.4\,mm^2$;

T-MR: tagged MR sequences in three orthogonal directions with reduced field-of-view enclosing the left ventricle were acquired (TR/TE = $7.0/3.2\,ms$, flip angle = $19{-}25°$, tag distance = $7\,mm$). The data for each tagging direction consisted of multiple 2D slices covering the whole LV volume. The typical spatial resolution in the plane orthogonal to the tagging direction is $\approx 1.0 \times 1.0\,mm^2$;

DE-MR: delayed-enhancement MR images were acquired 15 to 20 min following the administration of 0.1 to $0.2\,mmol/kg$ gadopentate dimeglumine (Magnevist, Bayer Healthcare, Dublin, Ireland) using conventional inversion recovery sequences. A multi-slice SA and three single-slice LA 2D images were acquired (TR/TE = $5.6/2.0\,ms$, flip angle = $25°$). The same field-of-view and orientation as the cine MR sequences was used. Slice thickness of both SA and LA images is $10\,mm$ with an in-plane resolution $\approx 1.4 \times 1.4\,mm^2$.
All images were acquired during sequential breath-holds of approximately $15\,s$ and were ECG-gated. Given their high in-plane spatial resolution, the cine

[1] Data were acquired from different projects and cannot be made publicly available due to lack of ethical approval or patient consent on data sharing.

MR images at end-diastole (ED) were employed to estimate LV geometry (see Sect. 3.1). The other cine MR images were not used in this work. An average high resolution $3D+t$ T-MR sequence was derived from the three T-MR acquisitions with orthogonal tagging directions and was used to estimate the LV deformation (see Sect. 3.1). Finally, the DE-MR images were used to estimate the location of LV scar. These scar maps were used in the training and validation of the classifier (see Sect. 3.2).

3 Methods

The main novelty of the proposed method lies in the application of dictionary learning to 3D LV motion descriptors for classification of scarred myocardium. An illustration of the proposed framework is shown in Fig. 1. To allow motion comparison from different patients, a spatio-temporal motion atlas of the LV was generated similarly to [4]. The use of a spatio-temporal motion atlas allowed us to remove differences in LV anatomy and cardiac cycle duration from the comparison of LV motion.

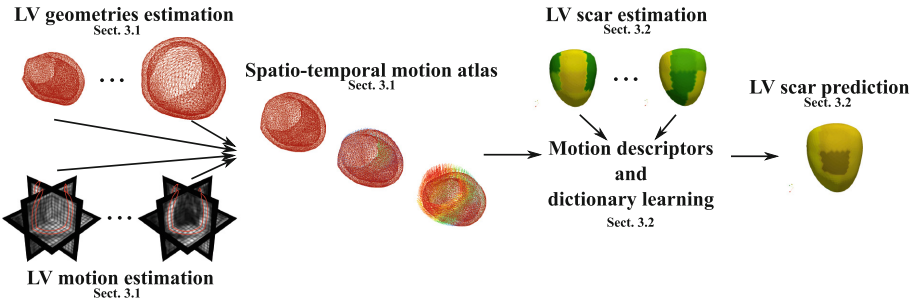

Fig. 1. Overview of the proposed framework.

3.1 Spatio-Temporal Motion Atlas

The formation of the LV spatio-temporal motion atlas comprises estimation of LV geometry and motion, spatial normalisation of LV geometries and motion reorientation from each subject-specific to the common atlas coordinate system.

Prior to the LV geometry and motion estimation, the SA and LA cine MR sequences were spatially aligned to the T-MR coordinate system, as in [11].

LV Geometry Estimation. For each patient, the end-diastolic (ED) cardiac phase was chosen as the temporal reference. The LV myocardium, excluding papillary muscles, was manually segmented from the ED frames of the multi-slice SA and three LA cine MR images. The four binary masks were fused together into an isotropic $2\,mm^3$ binary image and the result was further refined manually to

obtain a smooth LV segmentation. To determine point correspondences amongst all LV geometries, an open-source statistical shape model (SSM) of the LV was employed [6]. The SSM represents the anatomical variance of a population of 134 patients and consists of the epi- and endo-cardial surfaces. After an initial landmark-based rigid alignment, the modes of variation of the SSM were optimised to maximise the overlap between the LV segmentation and the volume of the SSM. Non-rigid registration followed the mode optimisation to refine local alignment. An example of a resulting LV surface is shown in Fig. 2(a), (b), (c), (d), (e), (f) and (g).

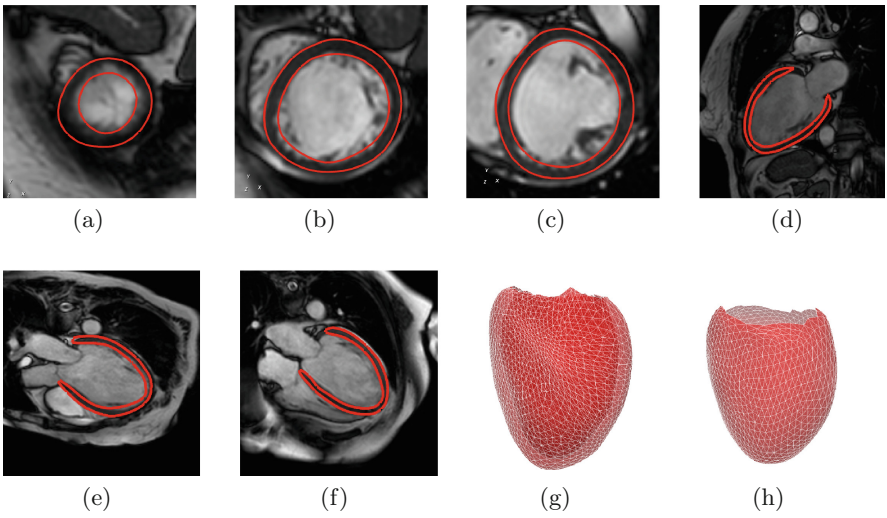

Fig. 2. Example of estimated LV anatomical surface at end-diastole. The estimated LV mesh is overlaid onto a (a) apical, (b) mid and (c) basal cine SA slice and (d) 2-chamber, (e) 3-chamber, and (f) 4-chamber cine LA slices. Figure (g) shows the resulting SSM epi- and endo-cardial meshes, while (h) shows the resampled medial LV mesh.

To facilitate the computation of motion descriptors, a medial surface mesh with regularly sampled vertices (≈1500) was generated from the personalised SSM epi- and endo-cardial surfaces. An example of a resampled medial surface is shown in Fig. 2(h). The same resampling strategy was employed for all patients to maintain point correspondence.

LV Motion Estimation. As mentioned in Sect. 2, an average high resolution $3D{+}t$ T-MR sequence was derived from the $3D{+}t$ T-MR sequences with orthogonal tagging planes. For each patient, the trigger time t_T specified in the DICOM meta-tag of the T-MR volumes was normalised with respect to the patient's average cardiac cycle, such that $t_T \in [0, 1)$, with 0 being ED. A $3D + t$ free-form-deformation algorithm with sparse spatial and temporal constraints [12] was employed to estimate LV motion with respect to the ED cardiac phase.

This algorithm estimates a smooth and continuous $3D + t$ transformation for any $t \in [0, 1)$. This way, temporal normalisation was achieved for each patient, regardless of the number of acquired T-MR volumes and cycle length.

Spatial Normalisation. Spatial normalisation aims to remove bias towards patient-specific LV geometries from the motion analysis. LV surfaces at ED (see Fig. 2(h)) were derived from N patients using the steps outlined above. An initial Procrustes alignment based on the point correspondences was performed on the N medial LV surfaces, obtaining a set of affine transformations $\{\phi^n_{aff}\}, n = 1, \ldots, N$ with respect to a randomly chosen reference. An average surface was computed from the aligned surfaces and an unbiased LV medial surface was computed by transforming the average surface by the inverse of the average affine transformation $\tilde{\phi}_{aff} = \frac{1}{n}\sum_n \phi^n_{aff}$. This way, bias towards the initial reference is removed. An example of an unbiased LV surface is shown in Fig. 3(b). The original transformations $\{\phi^n_{aff}\}$ were similarly normalised to enforce an average similarity transformation equal to identity $\hat{\phi}^n_{aff} = \phi^n_{aff} \circ (\tilde{\phi}_{aff})^{-1}$. To capture the local differences in LV geometry, all surfaces were consequently aligned to the unbiased medial LV surface using Thin Plate Spline (TPS) transformations $\{\phi^n_{TPS}\}$. The resulting transformation from the patient-specific coordinate system to the unbiased LV surface is given by $\phi^n = \phi^n_{TPS} \circ \hat{\phi}^n_{aff}$ [4].

Motion Reorientation. To compare cardiac phases amongst all patients, the reference ED medial surface was warped to $T = 24$ cardiac phases equally distributed in $[0, 0.8]$ by using the estimated $3D+t$ transformation for each patient. Only the first 80 % of the cardiac cycle was considered since it is the typical coverage of T-MR sequences, and the estimated motion for $t \in (0.8, 1]$ is therefore due to motion interpolation. As a result, the patient-specific LV motion was fully represented by the T shapes. We denote with $\mathbf{v}^n_{p,t} = \mathbf{u}^n_{p,t} - \mathbf{u}^n_{p,0}$ the motion at location $\mathbf{u}$ of vertex $p \in 1, .., P$ at the cardiac phase $t \in 1, .., T$ with respect to the ED phase for patient $n \in 1, .., N$. The aim of motion reorientation is to transport $\mathbf{v}^n_{p,t}, \forall n, t, p$ from each patient specific coordinate system to the coordinate system of the unbiased average surface. Under a small displacement assumption [3,9], this is achieved by computing $\mathbf{v}^{atlas}_{n,p,t} = J^{-1}(\phi^n(\mathbf{u}_p)) \cdot \mathbf{v}^n_{p,t}$, where $J(\phi^n)$ denotes the Jacobian of the transformation ϕ^n [3,4,9]. After reorientation, LV motion from different patients can be directly compared at each vertex p of the unbiased LV medial surface and cardiac phase t.

3.2 Local Motion Descriptors

As a result of the previous steps, the LV motions $\mathbf{v}^{atlas}_{n,p,t}$, $\forall n, p, t$ are represented in a common coordinate system. For a better description of the LV motion, the atlas was segmented into the standard 16 AHA segments [2] (see Fig. 3(a) and (b)) and the LV motions $\mathbf{v}^{atlas}_{n,p,t}$ were decomposed into longitudinal, radial and circumferential cylindrical coordinates ($\mathbf{v}^{atlas}_{n,p,t} = [l_{n,p,t}, r_{n,p,t}, c_{n,p,t}]^T$) with respect to the long axis of the LV ED medial surface.

For each patient, the LV scar distribution was estimated from the SA and LA DE-MR images by using cmr[42] (Circle Cardiovascular Imaging Inc.). The software requires the observer to delineate the endo- and epi-cardial LV contours and to set an intensity threshold to best separate scarred from healthy myocardium. In this work, a single clinical expert derived the scar maps to eliminate inter-observer variability. Figure 3(c) shows an example of a resulting scar map, where the scar transmurality is specified for each AHA segment, while Fig. 3(d) shows the scar distribution mapped onto the unbiased LV atlas.

The aim of this work is to characterise scar as a function of the LV spatio-temporal motion information. To this end, as described in Guha *et al.* [5], local motion pattern (LMP) descriptors were computed from the spatio-temporal motion atlas to characterise the scar, and dictionary learning was subsequently employed on the LMP descriptors for classification. Finally, in order to robustly cope with outliers, a Random Sample Reconstruction [5] was employed to localise the scar of an unseen patient.

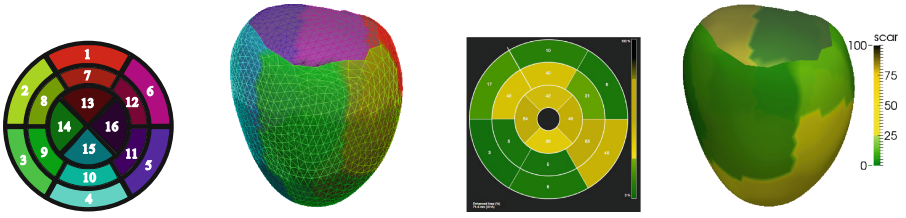

(a) (b) (c) (d)

Fig. 3. The standard AHA bull's eye plot (a) and the segmented unbiased LV medial mesh at ED (b). An example of scar distribution provided by the software cmr[42] and mapped onto the atlas is shown in (c)–(d)

Local Motion Pattern Descriptors. A LMP descriptor represents the local variations of the LV in the spatio-temporal dimensions [5]. After normalisation of the LV motions $\mathbf{v}_{n,p,t}^{atlas}$ with respect to the temporal norm $\|\mathbf{v}_{n,p}^{atlas}\|$, a neighbourhood B_p for each vertex p was considered. LMP descriptors were computed as the concatenation of the first 4 central temporal moments (mean, variance, skewness and kurtosis) for the circumferential, radial and longitudinal components for each point $p_i \in B_p$ at different temporal intervals (see Fig. 4). The three components were treated separately, as evidence has shown the different impact of the components on scar characterisation [7]. This results in a matrix $\mathbf{X} \in \mathbb{R}^{(M)\times(NP)}$, where M is proportional to the number of temporal intervals and the size of the neighbourhood (see Fig. 4). Given the high dimensionality of the LMP descriptors, Random Projections were used to reduce the complexity of the classification task, resulting in a matrix $\mathbf{\Psi} \in \mathbb{R}^{(D)\times(NP)}, D \ll M$, which contains projections of $\mathbf{X}$ onto a random D-dimensional subspace [5].

Concatenated Dictionary Learning. Dictionary learning (DL) techniques can learn an overcomplete set of basis functions (i.e. dictionary) to represent a signal with a high level of sparsity. DL has been employed successfully in many image processing tasks, including denoising, inpainting and classification.

In our context, the scar transmurality was divided into K evenly distributed classes within the $0-100\%$ scar transmurality range and the sparsity properties of DL were exploited for classification. In particular, a concatenated DL technique was employed under the hypothesis that LMP descriptors of scar class k are better represented by the corresponding dictionary rather than a dictionary of a different class. Therefore, class-specific dictionaries were trained by solving

$$\langle \mathbf{\Phi}_k, \mathbf{S}_k \rangle = \underset{\mathbf{\Phi}_k, \mathbf{S}_k}{argmin} \|\mathbf{\Psi}_k - \mathbf{\Phi}_k \mathbf{S}_k\|_2^2 + \alpha \|\mathbf{S}_k\|_1, \tag{1}$$

where $\mathbf{\Psi}_k \in \mathbb{R}^{(D)\times(NP)_k}$, $\mathbf{\Phi}_k \in \mathbb{R}^{(D)\times(A)}$ and $\mathbf{S}_k \in \mathbb{R}^{(A)\times(NP)_k}$ respectively are the descriptor matrix, the dictionary and the sparse code for the scar class k, while A is the number of basis functions (i.e. atoms) and $(NP)_k$ is the number of points belonging to the scar class k. We denote by $\langle .. \rangle$ the variables being optimised. The $scikit-learn$ python package was used for the code implementation and a least angle regression method was used to solve the lasso problem. After training, the K dictionaries were concatenated into a single dictionary $\mathbf{\Phi}_C = [\mathbf{\Phi}_1|...|\mathbf{\Phi}_K]$ and, provided with a set of unseen descriptors $\mathbf{\Psi}_{un}$, the sparse code $\mathbf{S}_{un}$ was computed using the Orthogonal Matching Pursuit (OMP) greedy algorithm for the optimisation of

$$\langle \mathbf{S}_{un} \rangle = \underset{\mathbf{S}_{un}}{argmin} \|\mathbf{\Psi}_{un} - \mathbf{\Phi}_C \mathbf{S}_{un}\|_2^2, \quad s.t. \quad \|\mathbf{s}_{un}\|_0 \leq \beta. \tag{2}$$

The sparse code $\mathbf{S}_{un}$ is the concatenation of $[\mathbf{S}_{\mathbf{\Phi}_1}|...|\mathbf{S}_{\mathbf{\Phi}_K}]$ where $\mathbf{S}_{\mathbf{\Phi}_k}$ is the sparse code corresponding to $\mathbf{\Phi}_k$. The estimated scar class is

$$k_e = \underset{i \in 1,..,K}{argmax} \|\mathbf{S}_{\mathbf{\Phi}_i}\|_0, \tag{3}$$

where $\|\mathbf{S}_{\mathbf{\Phi}_i}\|_0$ counts the non-zero entries of $\mathbf{S}_{\mathbf{\Phi}_i}$ [5].

Since the scar size can vary within a given AHA segment, the classification was performed using a Random Sample Reconstruction (RSR) [5], where the class k_e is assigned to the AHA segment if a randomly chosen subset of descriptors also belongs to the same class. RSR provides robustness to the classification, allowing classification of whole AHA segments based on a smaller set of descriptive points, as is the case for localised scarred myocardium (see [5] for details).

4 Experiments and Results

Given the low number of datasets containing scar in the apical and basal segments, the AHA segments corresponding to the LV mid cavity only (i.e. segments 7 to 12) were analysed. On average, each segment contained ≈ 100 points. For

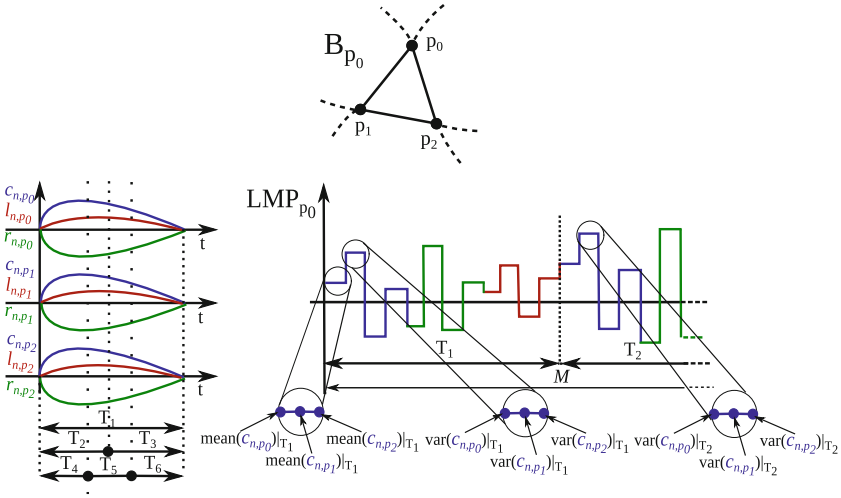

Fig. 4. Toy example of LMP descriptor computation for a neighbourhood composed of 3 points ($B_{p_0} = 3$). The descriptor is derived by concatenating the first four central moments of the circumferential (blue), radial (green) and longitudinal (red) components for each $p_i \in B_p, i = 1, 2, 3$ computed over 6 temporal intervals $T_j, j = 1, ..6$ (Color figure online).

simplicity, a binary classification (i.e. K=2, 0 - no scar, 1 - scar) was considered. The distribution of the binary ground-truth scar over all patients within the considered segments is shown in Fig. 5(a).

A leave-one-out cross validation was employed. Given the high number of free parameters for our technique, the best set was determined empirically, since an exhaustive search proved to be cumbersome. The set of parameters used was: $B_p = 8, j = 6$ temporal intervals (see Fig. 4), $D = 256$, sparsity coefficient $\alpha = .5$, maximum number of iterations = 200, number of atoms $A = 512$, number of non-zero coefficients in OMP $\beta = 2$. For the RSR, random set size ≈ 5 descriptors, probability of selecting an error-free set of points $P = .9$ (see [5]).

Results of the binary classification are reported in Fig. 5 considering each segment as an independent observation. Values of sensitivity, specificity, positive predictive value (PPV) and negative predictive value (NPV) achieved were 80 %, 87 %, 36 % and 98 %, respectively.

5 Discussion

In this paper, a novel framework for LV scar location using local motion descriptors has been proposed. Results on a cohort of 20 patients enrolled for CRT treatment were presented, with a sensitivity and specificity of 80 % and 87 % in a binary scar classification setting. Although the investigation presented in this paper is preliminary, to the authors' knowledge this is the first work to demonstrate that scar can be localised using motion information alone. Therefore, this

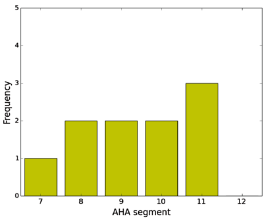

(a)

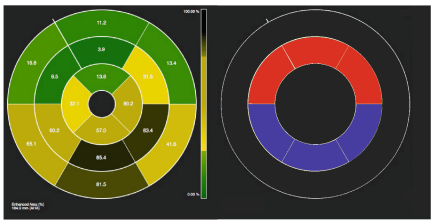

(b)

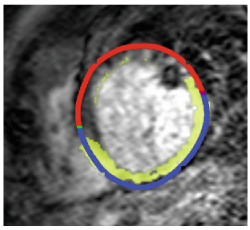

(c)

		GT		
		0	1	
PT	0	96	2	98
	1	14	8	22
		110	10	

Fig. 5. (a) Scar distribution over AHA segments 7–12 (mid LV cavity). (b) Bull's eye plot of a GT map and predicted scar (0 - red, 1 - blue), mid-cavity segments only. (c) the corresponding predicted scar mapped onto the medial surface is overlaid onto the SA DE-MR image (the LV scar in yellow). (Bottom right) Joint frequency table of AHA segment classification (GT - ground-truth, PT - proposed technique) (Color figure online).

represents an important proof-of-principle that such a technique may one day aid or even replace DE-MR in LV scar localisation and quantification.

There are a number of areas for future investigation before this possibility might become reality. One is the use of a larger number of scar classes (i.e. not a binary classification), or even a regression-based approach in which scar transmurality is directly predicted from the LMP descriptors. Further work is also required to refine the localisation of the ground truth scar, in which transmurality is currently assigned for all points within a segment. Moreover, inter- and intra- observer variability in the determination of scar transmurality needs to be investigated. Finally, investigations using larger numbers of scar-affected datasets is required.

Acknowledgements. This work was funded by EPSRC Grants EP/K030310/1 and EP/K030523/1. We acknowledge financial support from the Department of Health via the NIHR comprehensive Biomedical Research Centre award to Guy's & St Thomas' NHS Foundation Trust with KCL and King's College Hospital NHS Foundation Trust.

References

1. Bilchick, K.C., Kuruvilla, S., Hamirani, Y.S., Ramachandran, R., Clarke, S.A., Parker, K.M., Stukenborg, G.J., Mason, P., Ferguson, J.D., Moorman, J.R., Malhotra, R., Mangrum, J.M., Darby, A.E., DiMarco, J., Holmes, J.W., Salerno, M., Kramer, C.M., Epstein, F.H.: Impact of mechanical activation, scar, and electrical timing on cardiac resynchronization therapy response and clinical outcomes. J. Am. Coll. Cardiol. **63**(16), 1657–1666 (2014)
2. Cerqueira, M.D., Weissman, N.J., Dilsizian, V., Jacobs, A.K., Kaul, S., Laskey, W.K., Pennell, D.J., Rumberger, J.A., Ryan, T., Verani, M.S.: Standardized myocardial segmentation and nomenclature for tomographic imaging of the heart. Circulation **105**(4), 539–542 (2002)
3. Chandrashekara, R., Rao, A., Sanchez-Ortiz, G.I., Mohiaddin, R.H., Rueckert, D.: Construction of a statistical model for cardiac motion analysis using nonrigid image registration. In: Taylor, C.J., Noble, J.A. (eds.) IPMI 2003. LNCS, vol. 2732, pp. 599–610. Springer, Heidelberg (2003)
4. De Craene, M., Duchateau, N., Tobon-Gomez, C., Ghafaryasl, B., Piella, G., Rhode, K.S., Frange, A.: SPM to the heart: Mapping of 4D continuous velocities for motion abnormality quantification. In: Proc. of IEEE ISBI, pp. 454–457 (2012)
5. Guha, T., Ward, R.: Learning sparse representations for human action recognition. IEEE Trans. Pattern Anal. Mach. Intell. **34**(8), 1576–1588 (2012)
6. Hoogendoorn, C., Duchateau, N., Sanchez-Quintana, D., Whitmarsh, T., Sukno, F., De Craene, M., Lekadir, K., Frangi, A.: A high-resolution atlas and statistical model of the human heart from multislice CT. IEEE Trans. Med. Imaging **32**(1), 28–44 (2013)
7. Maret, E., Todt, T., Brudin, L., Nylander, E., Swahn, E., Ohlsson, J., Engvall, J.: Functional measurements based on feature tracking of cine magnetic resonance images identify left ventricular segments with myocardial scar. Cardiovasc. Ultrasound **7**(1), 53 (2009)
8. Medrano-Gracia, P., Suinesiaputra, A., Cowan, B., Bluemke, D., Frangi, A., Lee, D., Lima, J., Young, A.: An atlas for cardiac MRI regional wall motion and infarct scoring. In: Camara, O., Mansi, T., Pop, M., Rhode, K., Sermesant, M., Young, A. (eds.) STACOM 2012. LNCS, vol. 7746, pp. 188–197. Springer, Heidelberg (2013)
9. Rao, A., Chandrashekara, R., Sanchez-Ortiz, G., Mohiaddin, R., Aljabar, P., Hajnal, J., Puri, B.K., Rueckert, D.: Spatial transformation of motion and deformation fields using nonrigid registration. IEEE Trans. Med. Imaging **23**(9), 1065–1076 (2004)
10. Shan, K., Constantine, G., Sivananthan, M., Flamm, S.D.: Role of cardiac magnetic resonance imaging in the assessment of myocardial viability. Circulation **109**(11), 1328–1334 (2004)
11. Shi, W., Zhuang, X., Wang, H., Duckett, S., Luong, D., Tobon-Gomez, C., Tung, K., Edwards, P., Rhode, K., Razavi, R., Ourselin, S., Rueckert, D.: A comprehensive cardiac motion estimation framework using both untagged and 3-D tagged MR images based on nonrigid registration. IEEE Trans. Med. Imaging **31**(6), 1263–1275 (2012)
12. Shi, W., Jantsch, M., Aljabar, P., Pizarro, L., Bai, W., Wang, H., O'Regan, D., Zhuang, X., Rueckert, D.: Temporal sparse free-form deformations. Med. Image Anal. **17**(7), 779–789 (2013)